The Astrophysical Journal, 856:118 (13pp), 2018 April 1 https://doi.org/10.3847/1538-4357/aab3e7

Molecular Gas Reservoirs in Cluster Galaxies at $z = 1.46$

Masao Hayashi[1], Ken-ichi Tadaki[1], Tadayuki Kodama[2], Kotaro Kohno[3,4], Yuki Yamaguchi[3], Bunyo Hatsukade[3], Yusei Koyama[5,6], Rhythm Shimakawa[1,7], Yoichi Tamura[8], and Tomoko L. Suzuki[1]
[1] National Astronomical Observatory of Japan, Osawa, Mitaka, Tokyo 181-8588, Japan; masao.hayashi@nao.ac.jp
[2] Astronomical Institute, Tohoku University, Aramaki, Aoba-ku, Sendai 980-8578, Japan
[3] Institute of Astronomy, Graduate School of Science, The University of Tokyo, 2-21-1 Osawa, Mitaka, Tokyo 181-0015, Japan
[4] Research Center for the Early Universe, Graduate School of Science, The University of Tokyo, 7-3-1 Hongo, Bunkyo-ku, Tokyo 113-0033, Japan
[5] Subaru Telescope, National Astronomical Observatory of Japan, 650 North A'ohoku Place, Hilo, HI 96720, USA
[6] Department of Astronomical Science, SOKENDAI (The Graduate University for Advanced Studies), Mitaka, Tokyo 181-8588, Japan
[7] UCO/Lick Observatory, University of California, 1156 High Street, Santa Cruz, CA 95064, USA
[8] Department of Physics, Nagoya University, Furo-cho, Chikusa-ku, Nagoya 464-8601, Japan
Received 2017 December 26; revised 2018 February 27; accepted 2018 March 1; published 2018 March 30

Abstract

We present molecular gas reservoirs of 18 galaxies associated with the XMMXCS J2215.9–1738 cluster at $z = 1.46$. From Band 7 and Band 3 data of the Atacama Large Millimeter/submillimeter Array, we detect dust continuum emission at 870 μm and the CO $J = 2$–1 emission line from 8 and 17 member galaxies, respectively, within a clustercentric radius of R_{200}. The molecular gas masses derived from the CO and/or dust continuum luminosities show that the fraction of molecular gas mass and the depletion timescale for the cluster galaxies are larger than expected from the scaling relations of molecular gas on stellar mass and offset from the main sequence of star-forming galaxies in general fields. The galaxies closer to the cluster center in terms of both projected position and accretion phase seem to show a larger deviation from the scaling relations. We speculate that the environment of the galaxy cluster helps feed the gas through inflow to the member galaxies and reduce the efficiency of star formation. The stacked Band 3 spectrum of 12 quiescent galaxies with $M_{\rm stellar} \sim 10^{11}\ M_{\odot}$ within $0.5R_{200}$ shows no detection of a CO emission line, giving the upper limit of molecular gas mass and molecular gas fraction to be $\lesssim 10^{10}\ M_{\odot}$ and $\lesssim 10\%$, respectively. Therefore, the massive galaxies in the cluster core quench the star formation activity while consuming most of the gas reservoirs.

Key words: galaxies: clusters: individual (XMMXCS J2215.9–1738) – galaxies: ISM – galaxies: star formation

1. Introduction

Quiescent galaxies dominate galaxy clusters in the local universe (e.g., Dressler et al. 1997; Peng et al. 2010; Scoville et al. 2013), which implies that the environment of galaxy clusters has an impact on the transition of star-forming galaxies to quiescent galaxies. Based on the Kennicutt–Schmidt relation (Schmidt 1959; Kennicutt 1998; Kennicutt & Evans 2012), demonstrating empirically that the gas content of galaxies is one of the most essential quantities that govern star formation activities in galaxies, better understanding the evolution of galaxies in galaxy clusters in terms of both star formation activity and gas content leads to identifying the environmental processes responsible for the quenching of star formation in galaxies.

Most star-forming galaxies in the local universe follow a tight positive correlation between star formation rate (SFR) and stellar mass, which is called a main sequence (MS) of star-forming galaxies (e.g., Daddi et al. 2007; Elbaz et al. 2007; Noeske et al. 2007; Renzini & Peng 2015). The gas fraction and star formation efficiency of galaxies can be responsible for deviation from the MS in the plane of SFR–$M_{\rm stellar}$, in the sense that starburst (passive) galaxies tend to have a larger (smaller) gas fraction and/or higher (lower) efficiency of star formation (Saintonge et al. 2012, 2016, 2017; Sargent et al. 2014). On the other hand, as long as we focus on star-forming galaxies, an environment where galaxies reside does not have a strong impact on the star-forming MS and the relationship between gas reservoirs and star formation activity (Peng et al. 2010; Koyama et al. 2017). These observational studies may suggest that star formation activity in most galaxies is governed not by external processes such as galaxy interaction but by internal factors such as a gas reservoir. However, since galaxies in the local clusters have already evolved, it is essential to investigate evolving cluster galaxies in the early universe to reveal how present-day quiescent galaxies quench star formation within the galaxy clusters.

Observations in the high-z universe have also been conducted actively, and it is found that an MS of star-forming galaxies exists at each redshift up to $z \sim 3$ or higher (e.g., Speagle et al. 2014; Whitaker et al. 2014; Schreiber et al. 2015). Now that it becomes possible to compile about three orders of magnitude measurements of molecular gas from individual galaxies and stacks at $z = 0$–4, scaling relations of the molecular gas fraction and depletion timescale on offset from the MS, i.e., stellar mass, SFR, and redshift, are constructed (Genzel et al. 2015; Scoville et al. 2017; Tacconi et al. 2018). The gas fraction of galaxies tends to be larger at higher redshifts (e.g., Tacconi et al. 2010, 2013; Geach et al. 2011; Saintonge et al. 2013; Scoville et al. 2017), as if it follows the redshift evolution of cosmic SFR density (Madau & Dickinson 2014), suggesting that the SFR of a galaxy with a given mass becomes larger in proportion to the gas fraction as the redshift increases. In spite of the remarkable recent progress, most of the observations of molecular gas at high redshifts have been limited to the galaxies in general fields (e.g., Magnelli et al. 2012; Carilli & Walter 2013; Walter et al. 2014; Genzel et al. 2015; Silverman et al. 2015; Decarli et al. 2016a, 2016b; Seko et al. 2016; Scoville et al. 2017; Tacconi et al. 2018). An increasing number of studies have

surveyed molecular gas in galaxy (proto-)clusters at high redshifts of $z \approx 1$–3; however, the measurements of the gas content are at most for a few member galaxies in each cluster (Aravena et al. 2012; Wagg et al. 2012; Casasola et al. 2013; Ivison et al. 2013; Tadaki et al. 2014; Chapman et al. 2015; Wang et al. 2016; Dannerbauer et al. 2017; Lee et al. 2017; Noble et al. 2017; Rudnick et al. 2017; Stach et al. 2017; Webb et al. 2017).

The XMMXCS J2215.9–1738 galaxy cluster at $z = 1.457$ ($22^{\rm h}15^{\rm m}58\overset{\rm s}{.}5$, $-17°38'02\overset{''}{.}5$; Stanford et al. 2006) is one of the best targets to probe the early phase of environmental effects on molecular gas properties in cluster galaxies. This is because, in addition to previous studies indicating that massive galaxies in the cluster core are still in their formation phase (Hayashi et al. 2010, 2014; Hilton et al. 2010; Ma et al. 2015), CO $J = 2$–1 ($\nu_{\rm rest} = 230.538$ GHz, hereafter CO(2–1)) emission lines are found with the Atacama Large Millimeter/submillimeter Array (ALMA) from 17 galaxies associated with the galaxy cluster (Hayashi et al. 2017). The accretion phases of the gas-rich member galaxies are discussed based on the phase space of relative velocity versus clustercentric distance. The galaxies with CO(2–1) detected disappear from the very center of the cluster, suggesting that the gas-rich galaxies have entered the cluster more recently than the gas-poor galaxies located in the virialized region of this cluster. Hayashi et al. (2017), for the first time, succeeded in detecting CO(2–1) emission lines from as many as 17 member galaxies in the cluster at $z = 1.46$. The next step to better understanding the evolution of cluster galaxies is to investigate their gas reservoirs and efficiency of star formation.

Stach et al. (2017) independently detected 14 1.25 mm dust continuum sources from their own ALMA data in the central region of the XMMXCS J2215.9–1738 cluster. Among them, 11 sources are confirmed to be cluster members, and six sources have both CO(2–1) and CO(5–4) emission lines detected. The detections of dust continuum and/or CO line are consistent with those reported by Hayashi et al. (2017). The ratio of CO luminosities from the different transitions in the cluster is similar to those for field galaxies at similar redshifts. Gas masses of $\sim$(1–2.5) $\times$ 10^{10} $M_\odot$ and a relatively short gas consumption timescale of $\sim$200 Myr are estimated for the galaxies under the assumption of a conversion factor of $\alpha_{\rm CO} = 1$. They argued that based on the line widths and luminosities of the two CO transitions, the CO(2–1) gas tends to be stripped from the galaxies rather than the CO(5–4) gas, which implies that an environmental process acts on the cluster galaxies.

In this paper, we present full discussions from our ALMA observations in Band 3 and Band 7 in the XMMXCS J2215.9–1738 galaxy cluster through two programs, 2015.1.00779.S and 2012.1.00623.S. The data in Band 3 and Band 7 allow us to detect CO(2–1) emission and dust continuum emission at 870 μm from cluster member galaxies, respectively. We use the ALMA data to investigate molecular gas reservoirs in the member galaxies and then discuss the evolution of their star formation activities in terms of star formation efficiency and gas consumption. The outline of this paper is as follows. In Section 2, the ALMA data, as well as ancillary data covering the optical to mid-infrared (MIR), are described. The source detection in the ALMA Band 7 data is performed, and the photometric catalog with multiband photometry is created. In Section 3, we derive the molecular gas mass from the ALMA data and discuss the fraction of molecular gas mass and depletion timescale for the cluster member galaxies in the central region. In Section 4, we compare our results with the scaling relation for field galaxies and the results of other clusters at $z \sim 1.6$ from the literature. We also discuss the molecular gas mass in quiescent galaxies in the very center by stacking the Band 3 data. Conclusions are shown in Section 5. Throughout the paper, the cosmological parameters of $H_0 = 70$ km s^{-1} Mpc^{-1}, $\Omega_m = 0.3$, and $\Omega_\Lambda = 0.7$, along with the Chabrier (2003) initial mass function (IMF), are adopted. The velocity dispersion of the cluster member galaxies is $\sigma = 720$ km s^{-1}, and the radius of the galaxy cluster is $R_{200} = 0.8$ Mpc (Hilton et al. 2010).

2. Data

2.1. ALMA Band 3

Hayashi et al. (2017) already reported the initial results from the Band 3 data. Since the details of the Band 3 data and source detection in the data are described in the paper, we briefly mention them in this section.

The Band 3 data are available in 2.33 arcmin^2 observed at three pointings, where an area within 0.5 R_{200} from the cluster center is almost covered. The spectral coverage is 93.03–94.86 GHz with a spectral resolution of 13.906 MHz ($\sim$12.5 km s^{-1}). Integration time is 1.04 hr for each pointing. The typical noise level of the mosaicked 3D cubes is 0.12 mJy beam^{-1} at velocity resolutions of 400 km s^{-1}. The synthesized beam size is $1\overset{''}{.}79 \times 1\overset{''}{.}41$.

We use `Clumpfind` (Williams et al. 1994) to search for emission lines on the data cube. The emission-line search is performed in the cubes with different velocity resolutions of 50, 100, 200, 400, and 600 km s^{-1}. We have detected 21 candidates at a signal-to-noise ratio of $>$5.0 in at least one velocity resolution, after excluding overlaps. We cross-match the detections in the ALMA data with the optical and near-infrared (NIR) data described in Section 2.3 to remove the possible false detections. Consequently, we conclude that 17 emission lines with counterparts in the optical–NIR data are secure detections. The spectroscopic redshifts (if any) and photometric information, such as colors, are fully consistent with the counterparts being the member galaxies. Note that the remaining four candidates are not detected in the 1.25 mm dust continuum data in ALMA Band 6 shown by Stach et al. (2017), and our ALMA Band 7 data described below are not available to them. The spectra, intensity maps, and properties of the individual 17 emission lines are shown in Hayashi et al. (2017). For cluster member galaxies without individual CO detection (Section 2.4), we estimate an upper limit of CO luminosity from a 5σ noise level in the cube with 400 km s^{-1} velocity resolution.

2.2. ALMA Band 7

The observations in Band 7 were conducted in 2015 July. Four spectral windows are set at central frequencies of 338, 340, 350, and 352 GHz with each bandwidth of 1.875 GHz. The data are taken at 10 pointings to target 13 [O II] emission-line galaxies (Hayashi et al. 2010) that have a dust-corrected SFR$_{\rm [O\,II]}$ of $>$93 $M_\odot$ yr^{-1}, which results in the patchy data coverage of 0.61 arcmin^2 (Figure 1). Integration time is 7.06 minutes for each pointing. The synthesized beam size is $0\overset{''}{.}181 \times 0\overset{''}{.}157$ with a position angle of $44\overset{\circ}{.}7$. The spatial

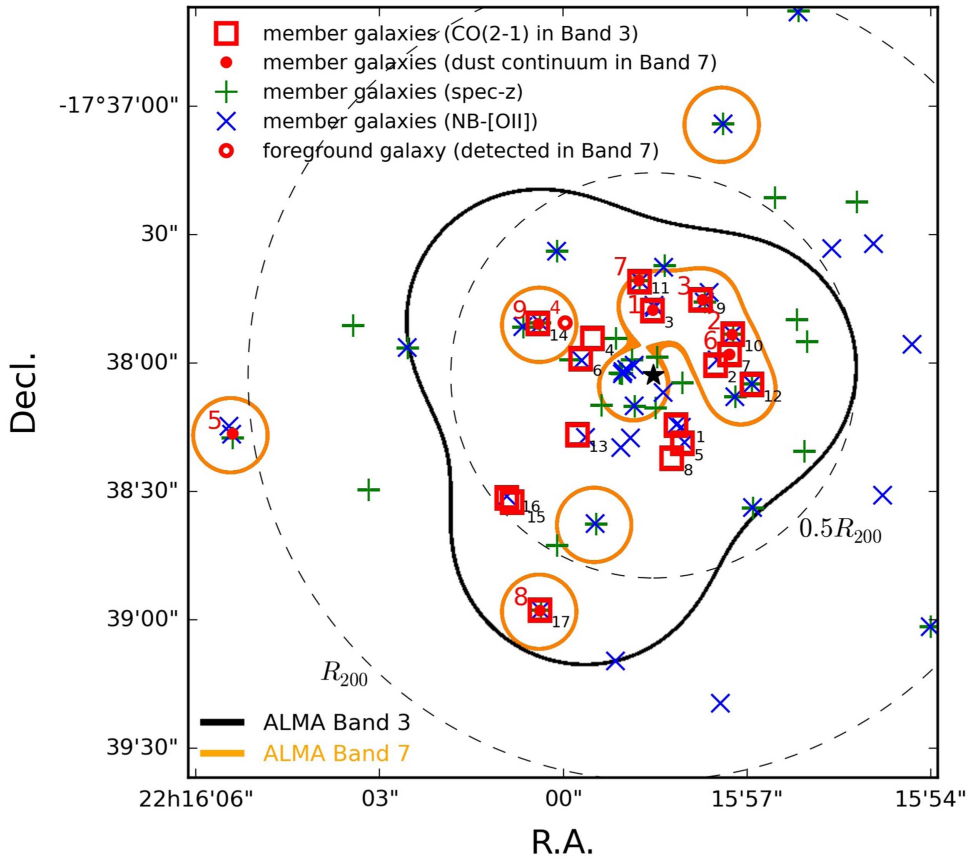

Figure 1. Spatial distribution of galaxies detected in the ALMA data. Filled red circles show the cluster member galaxies with dust continuum detected in Band 7. The open red circle also shows a Band 7 source, but it is a foreground galaxy at $z = 1.30$ (Stach et al. 2017). Open squares show the member galaxies with detection of the CO(2–1) emission line. The numbers next to the symbols are the IDs shown in Tables 1 and 2. The black (orange) curves show the area where Band 3 (7) data are available. The green and blue crosses show the member galaxies confirmed by spectroscopy and [O II] emitters associated with the cluster, respectively (Hilton et al. 2010; Hayashi et al. 2014; Beifiori et al. 2017). A star symbol shows a cluster center determined with extended X-ray emission (Stanford et al. 2006). The dashed circles show the clustercentric radius of $0.5R_{200}$ and R_{200} (Hilton et al. 2010).

resolution is comparable to optical–NIR data observed with the *Hubble Space Telescope* (*HST*).

Calibration of the raw data is conducted using the Common Astronomy Software Applications (CASA version 4.3.1; McMullin et al. 2007) with a standard ALMA pipeline. The Briggs weighting with a robust parameter of 2.0 (i.e., natural weighting) and a CLEAN threshold of 0.35 mJy ($\sim 5\sigma$) are adopted to make CLEANed images. Among 10 pointings, the data at five pointings nearest from the cluster center are mosaicked to make a single image (Figure 1). The typical noise levels of these images are 0.061–0.068 mJy beam^{-1}, which are measured by fitting a Gaussian to the histogram of pixel counts while ignoring the bright end of the histogram that some bright sources can contribute to.

We search for sources with a pixel count larger than 4.6σ in each image. We have detected nine sources at 870 μm from the Band 7 data, all of which have a counterpart in optical and NIR data (Figure 2). Similar to the 1.25 mm dust continuum sources reported by Stach et al. (2017), Figure 2 suggests that the several 870 μm dust continuum sources have an adjacent companion of a smaller object. The detection threshold lower than 4.6σ results in selecting sources without any counterpart in optical and NIR data, and thus they are likely to be spurious sources. This suggests that the threshold that we apply is reasonable. As another check of the reliability of the extracted sources, we also apply the same threshold to the inverted data to select pixels with a large negative value and then find only one negative detection. Therefore, we conclude that all of the detections are real (Table 1).

The flux densities of dust continuum emission are measured with a $0\farcs44$ (=22 pixels) diameter aperture, i.e., $\sim 2.4\times$ the beam size. The errors of the flux densities are estimated from the 10,000 measurements with the same aperture at the random positions over the individual images. The 1σ error is derived by fitting a Gaussian to the histogram of the random measurements. We also measure the flux densities in the uv-tapered map with the synthesized beam size of $0\farcs48 \times 0\farcs46$ to verify whether there is a flux of an extended component resolved out. The photometry is performed in the same manner as in the natural weighting map but for the $1\farcs0$ diameter aperture being used for the measurement in the tapered map. In the case that the measurement in the natural weighting map is consistent with that in the tapered map within the 1σ error, we use the flux densities measured in the natural weighting map. Otherwise, we use the measurement in the uv-tapered map. The flux densities measured are shown in Table 1.

The nine detections with $S_{\nu,870\,\mu\mathrm{m}} > 0.49$ mJy in 0.61 arcmin^2 suggest that the number density of the 870 μm sources in this region is a factor of 2–3 larger than expected from the cumulative number counts of ALMA dust continuum sources in deep general fields (e.g., Fujimoto et al. 2016; Hatsukade et al. 2016). However, since the patchy coverage of the ALMA Band 7 data does not cover the region where there are many cluster members, the number density would be a

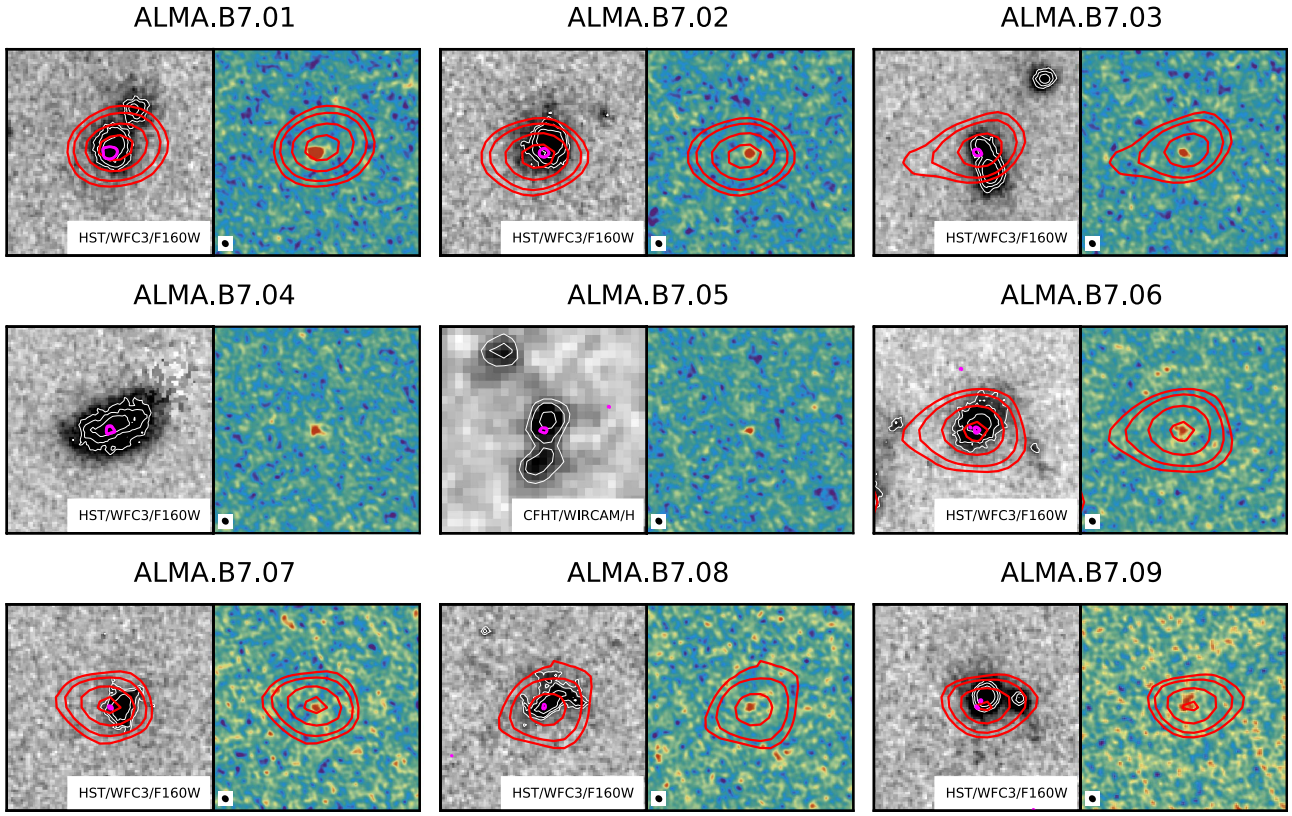

Figure 2. Postage stamps of the galaxies detected in ALMA Band 7, 5″ on a side. The right panels show the intensity map in Band 7, and the synthesized beam size is shown in black in the lower left corner. The left panels show the *H*-band image (*HST*/WFC3 F160W data, if available, otherwise CFHT/WIRCam *H*-band) along with the white contours of the 2σ, 3σ, and 5σ levels. They are also overlaid with magenta contours showing the Band 7 intensity map of 4.0σ, 4.5σ, and 5.0σ levels. The red contours in all panels show the intensity of the CO(2–1) emission lines (Hayashi et al. 2017). Note that ALMA.B7.04 is not a cluster member galaxy but a foreground galaxy (Table 1).

lower limit. Indeed, Stach et al. (2017) reported that the center of this cluster is an $\sim 7\times$ overdensity of 1.25 mm dust continuum sources.

Seven out of the nine sources have a counterpart of CO(2–1) emitters detected in the Band 3 data (Figure 2). Comparing the intensity map of CO(2–1) with the map of Band 7, the position of both dust continuum and CO emission coincides well. Also, the dust continuum emission comes from the compact region of the center of the individual galaxy, which is similar to the previous studies for high-z galaxies (Ikarashi et al. 2015; Simpson et al. 2015; Barro et al. 2016; Hodge et al. 2016; Chen et al. 2017; Tadaki et al. 2017). Although one source, B7.05, is located out of the Band 3 data coverage, it has a counterpart of [O II] emitters selected by Subaru/Suprime-Cam narrowband imaging (Hayashi et al. 2014). However, the source B7.04 is likely to be a foreground galaxy, judging from the appearance in the optical and NIR data (see also Stach et al. 2017, which shows that this is a galaxy at $z = 1.30$). Therefore, we regard the eight 870 μm sources as the cluster member galaxies. Combining the results of Hayashi et al. (2017), we have found 18 detections in total in the ALMA Band 3 and Band 7 data (see Figure 1 and Table 2).

2.3. Archival Imaging Data

We have optical images taken with the Subaru/Suprime-Cam in B, R_c, i', z', NB912, and NB921, which are used in our previous studies (e.g., Hayashi et al. 2010, 2014). Other imaging data in the optical-to-infrared (IR) wavelengths are retrieved from a public archive. The Canada–France–Hawaii Telescope Legacy Deep Survey (CFHTLS-Deep) provides us with the complementary optical images taken with the CFHT/MegaCam in u^* and g', and the WIRCam Deep Survey (WIRDS; Bielby et al. 2012) provides us with the NIR images taken with the CFHT/WIRCam in J, H, and K_s, all of which are retrieved from the CFHT Science Archive. Other NIR images taken with the Wide Field Camera 3 (WFC3) on *HST* in the F125W, F140W, and F160W filters (Beifiori et al. 2017) are also retrieved from the *HST* archive. The MIR data of *Spitzer*/IRAC 3.6–5.8 μm and MIPS 24 μm (Hilton et al. 2010) are retrieved from the Spitzer Heritage Archive (SHA). We do not use IRAC 8.0 μm data because they are not deep, and thus many cluster members seem not to be detected in 8.0 μm.

A coadd image in MIPS 24 μm is created by us from the Basic Calibrated Data (BCD) products retrieved from the archive. This is because some pixels suffer from soft saturation in the individual BCD products (see Hilton et al. 2010 for details); thus, the image quality at the north side is not good in the MIPS 24 μm image reduced by the standard pipeline, which can be retrieved from the archive. Therefore, we mask the regions suffering from soft saturation in the individual frames and then coadd them with the MOsaicker and Point source EXtractor (MOPEX). Also, the pixel scale is set to be $1\farcs25$ pixel^{-1}.

2.4. Catalogs of Cluster Member Galaxies

In addition to the sample of 18 ALMA sources, we have other catalogs of cluster member galaxies selected from

Table 1
Properties of Galaxies Detected in ALMA Band 7

ID	R.A. (J2000)	Decl. (J2000)	S/N[a]	$S_{\nu,870\,\mu m}$ (mJy)	Detection[b] in 1.25 mm	Counterpart
ALMA.B7.01	22 15 58.53	−17 37 47.6	17.4	2.58 ± 0.23[c]	∘ (3)	NB921 [O II]
ALMA.B7.02	22 15 57.24	−17 37 53.4	10.2	1.08 ± 0.13	∘ (6)	NB912+NB921 [O II]
ALMA.B7.03	22 15 57.72	−17 37 45.2	10.0	0.71 ± 0.13	⋯	NB912+NB921 [O II]
ALMA.B7.04	22 15 59.97	−17 37 50.6	7.4	1.27 ± 0.18	∘ (4)	Foreground galaxy ($z = 1.30$)[d]
ALMA.B7.05	22 16 05.40	−17 38 16.5	7.1	0.49 ± 0.14	—	NB912+NB921 [O II]
ALMA.B7.06	22 15 57.29	−17 37 58.0	6.1	1.12 ± 0.23[c]	∘ (7)	sBzK
ALMA.B7.07	22 15 58.77	−17 37 40.8	4.8	0.70 ± 0.20	∘ (1)	NB912+NB921 [O II]
ALMA.B7.08	22 16 00.38	−17 38 57.9	4.7	0.51 ± 0.14	—	NB912+NB921 [O II]
ALMA.B7.09	22 16 00.40	−17 37 50.8	4.7	1.05 ± 0.24[c]	∘ (5)	NB912 [O II]

Notes.
[a] The signal-to-noise ratio in source detection.
[b] The numbers in parentheses show the ID of the 1.25 mm sources detected with ALMA Band 6 data by Stach et al. (2017). A "⋯" means nondetection in the data, while a "—" means that the data are not available for the galaxy.
[c] The uv-tapered map is used for the measurement of flux density. See the text for details.
[d] The redshift is from Stach et al. (2017).

previous studies (Hayashi et al. 2010, 2011, 2014; Hilton et al. 2010; Beifiori et al. 2017). The catalogs consist of [O II] emission-line galaxies selected from imaging with two narrowband filters (Hayashi et al. 2010, 2014) and galaxies confirmed by optical and NIR follow-up spectroscopy (Hilton et al. 2010; Hayashi et al. 2011, 2014; Beifiori et al. 2017). The catalogs provide us with an additional 47 member galaxies within a radius of $1.1 \times R_{200}$ (Figure 1), where there are 31 [O II] emission-line galaxies and 32 spectroscopically confirmed galaxies. Note that the 16 galaxies in the sample of [O II] emitters overlap with those in the sample of spectroscopically confirmed galaxies. Therefore, we can use the sample of 65 cluster member galaxies within a clustercentric radius of $\sim R_{200}$ in this study. The spatial distribution of the member galaxies is shown in Figure 1.

2.4.1. Multiband Photometry

Photometry in the optical, NIR, and MIR data is conducted for the ALMA sources, as well as the other cluster member galaxies. `SExtractor` (Bertin & Arnouts 1996) is used for photometry in the optical, NIR, and IRAC data. Since the seeing of the Subaru images is 1.″09, which is worse than that of the other images (Hayashi et al. 2014), we match the point-spread function (PSF) between the optical and NIR images. Note that we do not match the PSF of the IRAC images. This is because the PSF of IRAC data is quite different from that of optical or NIR data, and thus it is not advisable to match the PSF of optical and NIR data to that of IRAC data. We run `SExtractor` in double-image mode. The H-band images with better seeing before the PSF is matched, i.e., WFC3/F160W if available, otherwise WIRCam/H, are used as a detection image. For the photometry in the optical and NIR data, we measure the magnitudes of the galaxies with a 2″ diameter aperture and correct them for the aperture correction by 0.43 mag, which is estimated from the growth curve of a PSF to derive total magnitudes. The magnitudes are also corrected for Galactic absorption, assuming the extinction law of Cardelli et al. (1989). For the photometry in the IRAC data, magnitudes are measured with a 3″ diameter aperture, and then we apply the aperture correction of 0.54, 0.63, and 0.83 mag in [3.6], [4.5], and [5.8] to estimate the total magnitude.

We conduct PSF-fitted photometry with `IRAF/DAOPHOT` in the MIPS data according to the previous studies (e.g., Magnelli et al. 2009). We use the IRAC 3.6 μm data as a reference image. We fit the PSF to the MIPS data in each position of the IRAC 3.6 μm sources and measure the flux in 24 μm. We check the residual image to make sure that the fitting works well. We apply the aperture correction of 0.53 mag which is estimated from the growth curve of a PSF. To combine the photometry in the MIPS data with that in the shorter wavelengths, an aperture with a 1.″5 radius is used for the source matching. Seven of the 18 ALMA sources are detected in 24 μm (Table 2).

2.4.2. Stellar Mass, SFR, and Rest-frame Colors

The multiband photometry covering the optical-to-MIR wavelengths is used to estimate the stellar masses and SFRs of the galaxies. We use the C++ version[9] of the `FAST` code (Kriek et al. 2009) to perform the spectral energy distribution (SED) fitting. The redshifts of the galaxies are fixed at those estimated from CO(2–1) lines, optical and NIR spectroscopy, and narrowband response functions, where the redshifts determined from the former have higher priority when the redshifts from several methods are available. The model SED templates of the galaxies are generated by the code of Bruzual & Charlot (2003). The star formation histories of the exponentially declining model are adopted, where we set an e-folding time of $\log(\tau/\mathrm{yr}) = 8.5$–$10.0$ with $\Delta\log(\tau/\mathrm{yr}) = 0.1$ (Wuyts et al. 2011). Ages of 0.1–10.0 Gyr are acceptable with a step of $\Delta\log(\mathrm{age}/\mathrm{yr}) = 0.1$. The extinction curve of Calzetti et al. (2000) is assumed, and A_V ranges from 0.0 to 3.0. Metallicity is fixed to the solar value. A Monte Carlo simulation is performed 100 times for each galaxy to estimate a 1σ error in stellar mass and SFR.

The intrinsic SFRs estimated are sensitive to the reliability of the correction for dust extinction. MIR data are useful to estimate a component of the SFR obscured by dust, which suggests that it is not easy to estimate the dust-obscured SFR from the rest-frame UV and optical data (Tadaki et al. 2017; Whitaker et al. 2017). Several studies in a galaxy cluster at $z \sim 0.4$ suggest that galaxies in higher-density regions tend to

[9] https://github.com/cschreib/fastpp

Table 2
Properties of the 18 Galaxies Detected in ALMA Band 3 and Band 7

ID[a]			Redshift[b]	Star-forming or Quiescent[c]	$M_{\rm stellar}$ ($10^{10}\,M_\odot$)	$\rm SFR_{SED\text{-}fit}$ ($M_\odot\ \rm yr^{-1}$)	$f_{\nu,24\mu\rm m}$ (μJy)	$\rm SFR_{UV+24\,\mu m}$ ($M_\odot\ \rm yr^{-1}$)	$M_{\rm gas,CO}$ ($10^{10}\,M_\odot$)	$M_{\rm gas,dust}$ ($10^{10}\,M_\odot$)
	(B3)	(B7)								
ALMA.01	01	—	1.466	S	$8.13^{+0.78}_{-0.54}$	35^{+35}_{-2}	125 ± 10	91^{+7}_{-8}	$10.5^{+0.5}_{-0.7}$	—
ALMA.02	02	···	1.450	S	$3.39^{+0.69}_{-0.57}$	31^{+15}_{-13}	···	···	$2.7^{+0.6}_{-0.6}$	<3.7
ALMA.03	03	01	1.453	S	$11.22^{+0.26}_{-1.22}$	25^{+21}_{-6}	···	···	$10.7^{+0.8}_{-0.5}$	$13.8^{+1.0}_{-1.2}$
ALMA.04	04	—	1.466	S	$3.89^{+1.01}_{-0.65}$	$6^{+2.8}_{-2.9}$	···	···	$3.7^{+0.6}_{-0.7}$	—
ALMA.05	05	—	1.467	S	$2.29^{+0.66}_{-0.39}$	48^{+26}_{-20}	···	···	$3.1^{+0.6}_{-0.6}$	—
ALMA.06	06	—	1.467	S	$12.02^{+2.43}_{-0.80}$	145^{+69}_{-32}	180 ± 11	129^{+9}_{-6}	$10.5^{+0.7}_{-0.5}$	—
ALMA.07	07	06	1.452	S	$8.13^{+0.19}_{-0.72}$	35^{+49}_{-0}	···	···	$5.8^{+0.6}_{-0.6}$	$6.2^{+1.2}_{-1.3}$
ALMA.08	08	—	1.457	S	$5.75^{+0.27}_{-0.63}$	105^{+30}_{-34}	88 ± 10	65^{+8}_{-7}	$6.8^{+0.5}_{-0.6}$	—
ALMA.09	09	03	1.468	S	$10.72^{+0.25}_{-1.17}$	47^{+27}_{-24}	···	···	$3.5^{+0.5}_{-0.5}$	$3.8^{+0.7}_{-0.7}$
ALMA.10	10	02	1.454	S	$3.98^{+0.28}_{-0.43}$	72^{+28}_{-12}	125 ± 10	91^{+7}_{-8}	$8.1^{+0.6}_{-0.5}$	$6.8^{+0.8}_{-0.9}$
ALMA.11	11	07	1.451	S	$1.82^{+0.58}_{-0.75}$	17^{+29}_{-5}	···	···	$6.6^{+0.8}_{-0.9}$	$5.1^{+1.5}_{-1.4}$
ALMA.12	12	···	1.445	S	$1.48^{+0.22}_{-0.10}$	54^{+15}_{-11}	71 ± 10	58^{+7}_{-6}	$4.1^{+0.6}_{-0.5}$	<4.6
ALMA.13	13	—	1.471	S	$6.03^{+0.43}_{-2.71}$	21^{+55}_{-3}	60 ± 10	44^{+8}_{-6}	$5.8^{+0.7}_{-0.6}$	—
ALMA.14	14	09	1.451	Q	$9.12^{+0.00}_{-1.88}$	$3^{+0.1}_{-2.5}$	···	···	$3.2^{+0.6}_{-0.6}$	$5.8^{+1.3}_{-1.3}$
ALMA.15	15	—	1.465	S	$3.63^{+1.74}_{-0.24}$	28^{+10}_{-18}	85 ± 11	62^{+8}_{-9}	$6.6^{+0.6}_{-0.9}$	—
ALMA.16	16	—	1.465	S	$3.09^{+0.30}_{-0.52}$	37^{+29}_{-11}	···	···	$8.5^{+0.6}_{-0.9}$	—
ALMA.17	17	08	1.460	S	$2.45^{+1.81}_{-0.46}$	123^{+51}_{-80}	···	···	$5.8^{+0.7}_{-0.6}$	$3.5^{+1.0}_{-1.0}$
ALMA.18	—	05	1.465	S	$2.51^{+0.80}_{-0.11}$	72^{+15}_{-35}	···	···	—	$3.4^{+1.0}_{-0.9}$

Notes.
[a] A "···" means nondetection in the data, while a "—" means that the data are not available for the galaxy (see Figure 1).
[b] The redshifts are derived from the CO emission lines for all but ALMA.18 (Hayashi et al. 2017). The redshift of ALMA.18 is from Hilton et al. (2010).
[c] The galaxies are classified as star-forming (S) or quiescent (Q) galaxies based on the rest-frame $U-V$ and $V-J$ colors (Figure 4).

be more dusty (Koyama et al. 2013; Sobral et al. 2016). Therefore, if a galaxy has a detection in 24 μm, we estimate the SFR from the combination of UV and IR luminosities. Otherwise, we use the dust-corrected SFR derived from the SED fitting described above. The IR luminosities are estimated from 24 μm fluxes using a conversion factor given by Wuyts et al. (2008), and the UV luminosities are estimated from the rest-frame 2800 Å luminosity of the best-fit SED. Then, using the equation given by Wuyts et al. (2011),

$$\frac{\rm SFR_{UV+IR}}{M_\odot\ \rm yr^{-1}} = 1.09\times10^{-10}\cdot\frac{L_{\rm IR}+3.3L_{2800}}{L_\odot}, \quad (1)$$

the UV+IR luminosities are converted to $\rm SFR_{UV+IR}$.

Table 2 lists the stellar masses and SFRs for the ALMA sources. Figure 3 shows the SFRs of the galaxies as a function of stellar mass. We also plot the MS at a redshift of $z\sim1.46$ from the literature (Speagle et al. 2014; Whitaker et al. 2014). Most of the galaxies detected in the ALMA data are located on or above the MS at the redshift (i.e., within ±0.2 dex or higher from the MS). The other ALMA sources below the MS are massive galaxies with $\gtrsim10^{10.6}\,M_\odot$.

Figure 4 shows the rest-frame $U-V$ versus $V-J$ colors of the member galaxies. The $U-V$ and $V-J$ colors are derived from the best-fit SED. According to Brammer et al. (2011), we use the response function of the U and V filters defined by Maíz Apellániz (2006) and the 2MASS J filter to calculate the colors. The UVJ diagram is widely used to distinguish quiescent galaxies from star-forming galaxies (e.g., Labbé et al. 2005; Williams et al. 2009). Almost all of the CO(2–1) lines and dust continuum emission are detected from star-forming galaxies. Along the sequence of the star-forming galaxies in the UVJ diagram, the ALMA sources tend to have redder colors, implying that the CO line and dust continuum emission are easier to detect from more dusty star-forming galaxies (e.g., Tadaki et al. 2015; Rudnick et al. 2017). On the other hand, few quiescent member galaxies have either CO line or dust continuum emission detected. Indeed, ALMA.14 is only classified as a quiescent galaxy (see also Table 2).

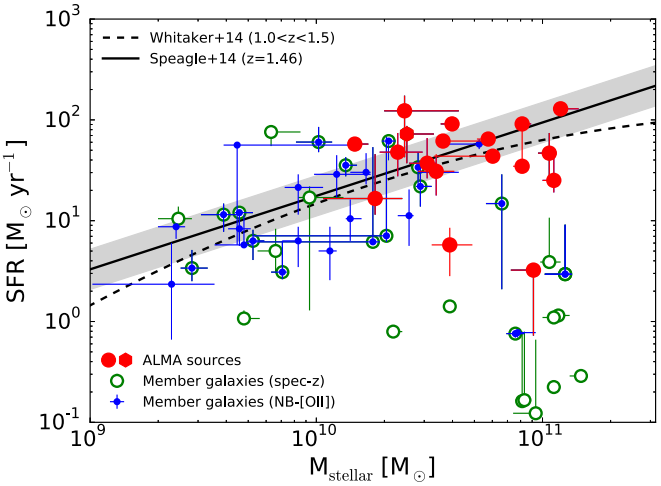

Figure 3. SFRs as a function of stellar mass for the cluster member galaxies within a radius of $\sim R_{200}$. The red symbols show the 18 ALMA sources: 17 CO(2–1) emitters are shown by circles, while the dust continuum source is shown by a hexagon. The spectroscopically confirmed galaxies are shown by green circles, and the [O II] emitters are shown by blue circles. The solid line with the gray region shows the MS with ±0.2 dex given by Speagle et al. (2014), and the dashed line shows the one by Whitaker et al. (2014).

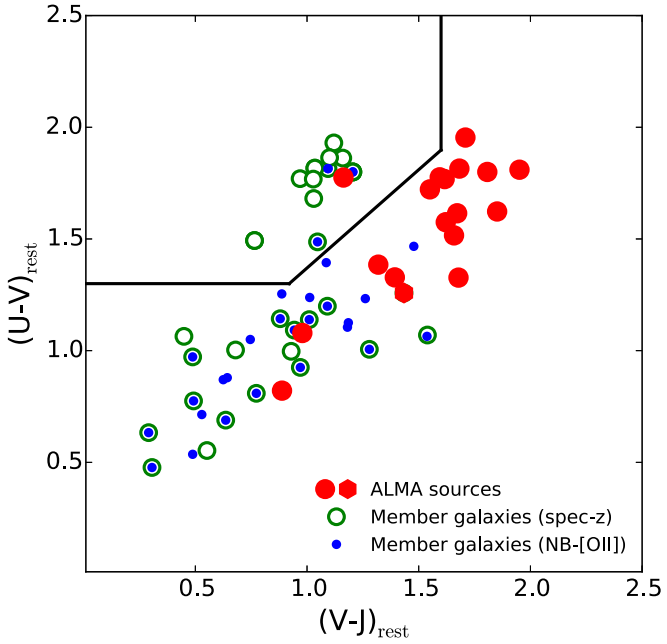

Figure 4. $U - V$ vs. $V - J$ colors in the rest frame. The symbols are the same as in Figure 3. The solid line is a boundary to distinguish quiescent galaxies from star-forming galaxies (Williams et al. 2009).

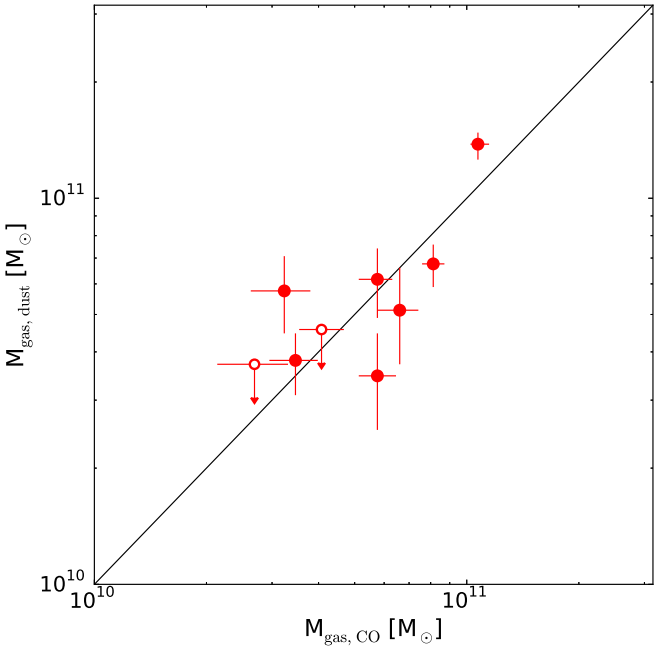

Figure 5. Comparison between molecular gas estimated from CO(2–1) and that from the dust continuum for galaxies in the area where both Band 3 and Band 7 data are available. The filled circles show the cluster members with both CO(2–1) line and dust continuum detected. The open circles show the members with CO(2–1) lines detected but dust continuum not detected. The upper limits are estimated from the flux densities of the 4.6σ noise level in the Band 7 data at the position of the CO(2–1) line, which is the same as the detection limit in Section 2.2.

3. Results

3.1. Molecular Gas Mass

We estimate the molecular gas mass from the luminosities of CO(2–1) emission line and dust continuum emission for the 18 cluster member galaxies with detections in the ALMA data. The CO(2–1) luminosities are derived in Hayashi et al. (2017) from the intensity map integrated in velocity by the width of the emission line ($2 \times$ FWHM). The luminosity, $L'_{\rm CO(2-1)}$, is in the range (4.5–22) $\times$ 10^9 K km^{-1} pc^2. The conversion factor from the CO luminosity to the molecular gas mass given by Tacconi et al. (2018) is adopted to estimate the molecular gas mass. We use $L'_{\rm CO(1-0)}/L'_{\rm CO(2-1)} = 1.2$ and $\alpha_{\rm CO(1-0)} = 4.36$. Note that the conversion factor is corrected for the metallicity dependence through the stellar mass–metallicity relation (Genzel et al. 2012; Bolatto et al. 2013); thus, the conversion factors that we adopt range from 4.99 to 7.31 and are dependent on the stellar mass. We also use Equation (16) of Scoville et al. (2016) to estimate the molecular gas mass from the dust continuum emission at 870 μm, where a dust temperature of $T_d = 25$ K is assumed and the metallicity- (i.e., stellar mass–) dependent ratio of molecular gas to dust mass is taken into account according to Tacconi et al. (2018).

Figure 5 compares the molecular gas mass from CO(2–1) luminosity with that from dust continuum luminosity for galaxies with a detection in both CO and the dust continuum. The molecular gas masses estimated from the two ways are consistent. Among the galaxies with a CO(2–1) line in the area covered by ALMA Band 7 data, two CO(2–1) emitters are not detected in Band 7. (The IDs are ALMA.02 and ALMA.12.) The two galaxies have the lowest CO(2–1) luminosities among the galaxies for which the Band 7 data are available. The 3.8σ source is seen in the Band 7 data near the position of ALMA.02, while no source at more than 3σ is seen around ALMA.12 within the synthesized beam of the Band 3 data. We plot their upper limit of the molecular gas mass from the dust continuum in Figure 5, suggesting that the gas mass from CO is not discrepant with the upper limit from the dust continuum for the two galaxies. Hereafter, if the galaxies have CO luminosity available, we use the gas mass derived from CO. Otherwise, we use the gas mass derived from the dust continuum; namely, we use $M_{\rm gas,dust}$ for the galaxy of ALMA.18 only. The molecular gas masses derived here are listed in Table 2. Moreover, we estimate an upper limit of the molecular gas mass from the upper limit of the CO luminosity (Section 2.1) for the individual member galaxies in the area covered by the Band 3 data.

The conversion factor applied to derive the molecular gas mass from the CO luminosity is one of the major uncertainties in the measurement. It is not obvious which conversion factors should be used. Stach et al. (2017) argued that at least two member galaxies in this cluster prefer the conversion factor $\alpha_{\rm CO} = 1$, based on the comparison between the gas mass from the CO luminosity and the dynamical mass from the width of the CO line. However, we find that the gas masses we estimate in the different ways, i.e., CO and dust continuum, are consistent with each other even for the two galaxies (ALMA.07 and ALMA.10 in Table 2). Moreover, we compare our results with the scaling relation for field galaxies given by Tacconi et al. (2018) in Section 4. The conversion factors that we apply in this work are the same as those in Tacconi et al. (2018), which enables a fair comparison of our results with the scaling relation.

Figure 6 shows the SFRs of the member galaxies as a function of molecular gas mass. There may be a mild trend that galaxies with larger gas masses have larger SFRs, although a larger sample is required for confirmation of this trend. At a given molecular gas, the galaxies can have a wide range of SFRs ($\sim$1.0 dex), indicating a wide range of star formation

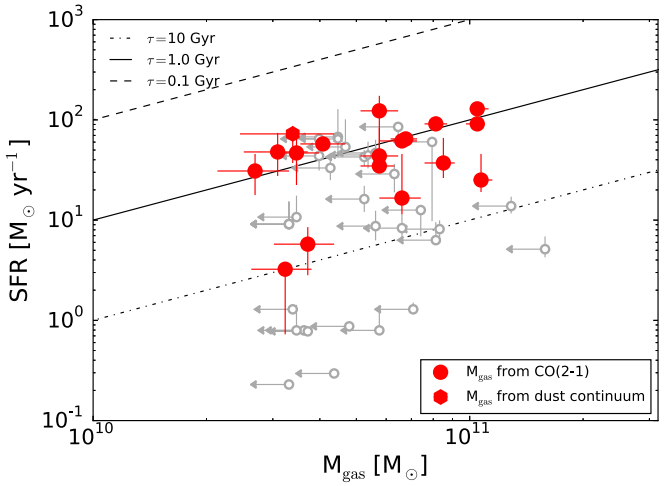

Figure 6. SFRs as a function of molecular gas mass. The red circles are 17 CO(2–1) emitters, and the red hexagon is the dust continuum source. The gray symbols show the upper limit of molecular gas at the SFR estimated. The dash-dotted, solid, and dashed lines show a constant depletion timescale, $\mathrm{SFR}/M_{\mathrm{gas}}$, of 10, 1.0, and 0.1 Gyr, respectively.

efficiency among the cluster member galaxies. The PHIBSS survey shows larger SFRs with ∼0.5 dex dispersion at a given molecular gas for field galaxies at $z = 1.0$–2.5 (Tacconi et al. 2013). These suggest that besides molecular gas, other factors also have an impact on the star formation activity of cluster galaxies.

3.2. Gas Mass Fraction and Depletion Timescale

The fraction of molecular gas mass to the sum of stellar and gas mass, $f_{\mathrm{gas}} = M_{\mathrm{gas}}/(M_{\mathrm{gas}} + M_{\mathrm{stellar}})$, and the depletion timescale, $\tau = M_{\mathrm{gas}}/\mathrm{SFR}$, are useful to characterize the evolutionary phases of the galaxies. The fraction of gas mass can imply how the member galaxies have gas reservoirs and then can proceed to form stars, and the depletion time is a timescale reflecting the efficiency of star formation in the galaxies. Since we expect that star-forming galaxies located in the central region of the cluster are good candidates for present-day massive early-type galaxies, it is important to investigate the fraction of gas mass and the depletion timescale for the member galaxies to discuss the evolution of the cluster galaxies.

We investigate how the gas fraction and depletion time are related to the evolution of cluster galaxies. Here we focus on the following four factors: stellar mass, offset from the MS of star-forming galaxies, clustercentric radius, and accretion phase based on phase space. The former two factors are related to the properties of the galaxies themselves. The stellar mass of galaxies is one of the most important properties showing the tight correlation with other galaxy properties, such as star formation, metallicity, and size. The offset of the MS is also an important factor to discuss the relation between the gas reservoirs and star formation activity in cluster galaxies. On the other hand, the latter two factors should give us insight into evolutionary processes peculiar to galaxy clusters after they belong to the galaxy cluster. A phase-space diagram is a useful tool to characterize the accretion state of cluster member galaxies relatively free from effects due to the 2D projected positions with respect to the cluster center (Noble et al. 2013; Muzzin et al. 2014; Jaffé et al. 2015; Noble et al. 2016). Hayashi et al. (2017) showed that the CO emitters tend to be distributed at the edge of the virialized region or in the region of relatively recent accretion. The galaxies with CO lines detected disappear from the very center of the cluster. They argue that the gas-rich galaxies with CO detections have spent only relatively short times within the cluster.

Figure 7 shows the gas fraction (f_{gas}) and depletion time (τ) of the 18 gas-rich member galaxies as a function of stellar mass, offset from the MS, clustercentric radius, and accretion phase. We assume the MS of star-forming galaxies at $z = 1.46$ given by Speagle et al. (2014), who investigated the evolution of the MS up to $z \sim 6$ by compiling 25 studies from the literature. The offset of the MS is derived from a difference between the SFR and the expectation from the MS at a given stellar mass. We also plot the upper limits of the gas fraction and depletion time for the other member galaxies.

The gas fractions in the massive galaxies with $M_{\mathrm{stellar}} \sim 10^{11}\,M_{\odot}$ are roughly less than half, and the depletion timescale is $\gtrsim$1 Gyr. In particular, these galaxies with $\Delta\mathrm{MS} < -1$ show a lower gas fraction of $<1/3$, suggesting that massive quiescent galaxies no longer have large gas reservoirs and efficient star formation in the cluster center. On the other hand, the galaxies above the MS show a larger gas fraction and smaller depletion timescale, as the offset from the MS is larger. The galaxies with a larger offset from the MS tend to be gas-rich galaxies forming stars in the starburst phase. As long as we focus on the galaxies with CO and dust continuum detected, most of them show $f_{\mathrm{gas}} \gtrsim 0.4$ and $\tau \gtrsim 1$ Gyr, and there is no strong dependence of gas fraction and depletion time on the clustercentric radius and accretion phase. However, it is also a fact that massive quiescent galaxies that show $f_{\mathrm{gas}} \lesssim 0.2$ and $\tau \sim 10$ Gyr exist in the cluster center. These are the few member galaxies with an intermediate gas fraction and depletion timescale. Some rapid processes may be able to reduce the gas reservoirs in cluster galaxies.

We integrate the molecular gas mass, stellar mass, and SFR for the member galaxies within a radius of $0.5R_{200}$ to estimate an average gas fraction, $\langle f_{\mathrm{gas}} \rangle = \sum M_{\mathrm{gas}}/\sum M_{\mathrm{stellar}}$, and an average depletion timescale, $\langle \tau \rangle = \sum M_{\mathrm{gas}}/\sum \mathrm{SFR}$, in the cluster. The gas fraction and depletion time are in the ranges $\langle f_{\mathrm{gas}} \rangle = 0.29$–$0.53$ and $\langle \tau \rangle = 0.83$–$2.3$ Gyr, where the upper limit is derived by taking account of the upper limit of the gas mass for the member galaxies without ALMA detection and the lower limit is derived by assuming no gas mass for these member galaxies.

4. Discussion

4.1. Comparison with the Scaling Relations

The scaling relations of the gas–to–stellar mass ratio ($M_{\mathrm{gas}}/M_{\mathrm{stellar}}$) and depletion timescale on both the specific SFR and its offset from the MS are derived by Tacconi et al. (2018) from the compilation of more than 1000 measurements of molecular gas mass for galaxies at $z = 0$–4 with a wide range of stellar mass and SFR. We use the scaling relations to compare our results with the representative populations in general fields at similar redshifts, where we assume the MS of Speagle et al. (2014) as in Tacconi et al. (2018). Figure 8 shows the ratio of the molecular gas fraction and depletion time to what is expected from the scaling relations as a function of stellar mass, offset from the MS, clustercentric radius, and accretion phase based on phase space.

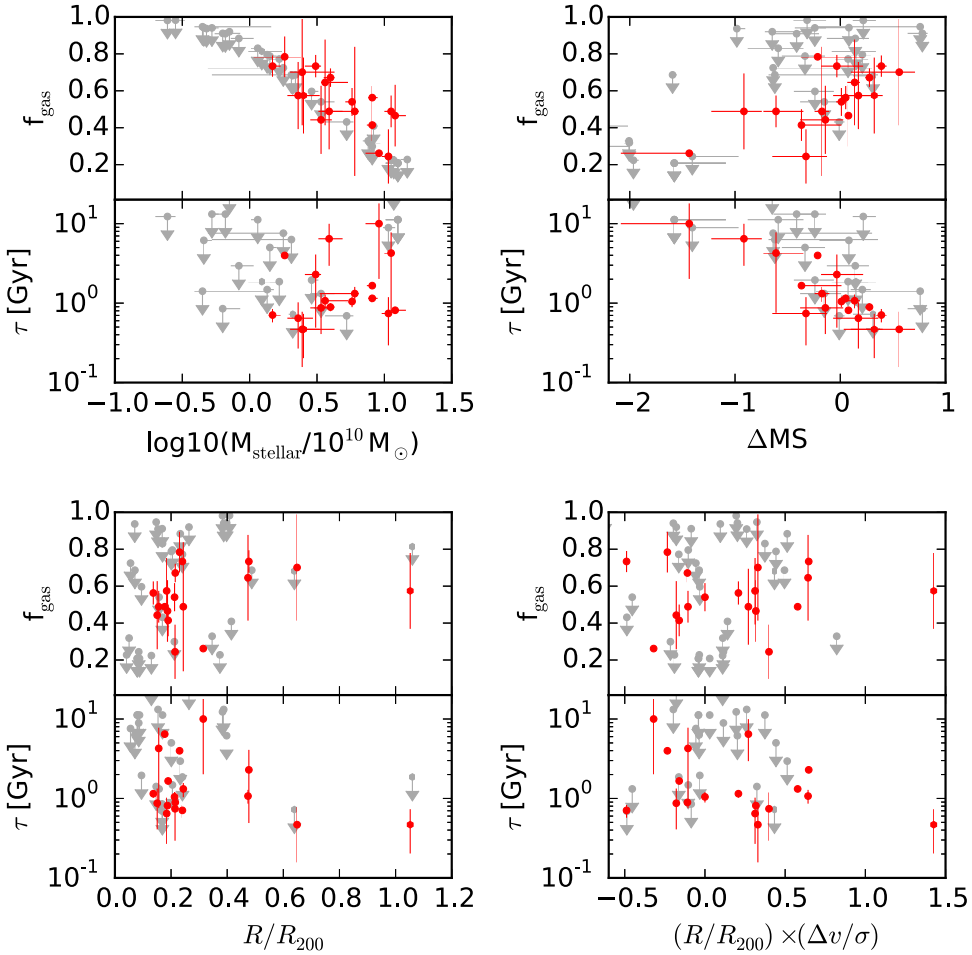

Figure 7. Molecular gas fraction, $f_{\rm gas} = M_{\rm gas}/(M_{\rm gas} + M_{\rm stellar})$, and depletion time, $\tau = M_{\rm gas}/{\rm SFR}$, of the cluster member galaxies as a function of stellar mass ($M_{\rm stellar}$), offset from the MS (ΔMS), clustercentric radius (R/R_{200}), and accretion phase ($(R/R_{200}) \times (\Delta v/\sigma)$), where we assume the MS of star-forming galaxies at $z = 1.46$ given by Speagle et al. (2014). The red symbols show the 18 ALMA sources detected in CO(2–1) or dust continuum. The gray symbols show the upper limit of the gas fraction and deletion time for the other member galaxies without detection in the ALMA data.

The member galaxies with CO and/or dust continuum detected in the cluster tend to have a larger gas fraction and depletion time compared with those from the scaling relations. The cluster galaxies with a large offset below from the MS also have a gas fraction larger than that for field galaxies; nevertheless, they are quenching star formation. Judging from the distribution of the cluster galaxies in the SFR–$M_{\rm stellar}$ diagram (Figure 3), the larger depletion timescale is due not to the lower SFR but to the larger amount of gas. The results may imply that the infalling regions and filaments around galaxy clusters are easier to feed gas to member galaxies, which results in the larger gas fraction in cluster galaxies. Also, some environmental effects peculiar to galaxies associated with galaxy clusters may reduce the efficiency of star formation. We speculate that shock-heating by ram pressure can be one of the causes of the low efficiency (Jáchym et al. 2014; Wong et al. 2014). Although the statistics is poor, it seems that the member galaxies in $R \gtrsim 0.5R_{200}$ or with phases accreting more recently have a gas fraction and depletion time consistent with the scaling relations. On the other hand, the member galaxies infalling closer to the cluster center can have a larger gas fraction and depletion time than the scaling relations. This supports that some environmental effects have impacted the galaxies while moving within the galaxy cluster. Moreover, if the negative feedback from active galactic nuclei (AGNs) and/or supernovae (SNe) works on the galaxies (Carniani et al. 2017), the efficiency of star formation would be further reduced, although some studies suggest the possibility of positive feedback by AGNs (Kakkad et al. 2017).

However, we cannot completely exclude the possibility that we overestimate the molecular gas mass. Although we use a conversion factor, $\alpha_{\rm CO}$, dependent on stellar mass (i.e., metallicity through the mass–metallicity relation), if the cluster galaxies have higher metallicity at a given stellar mass, then the actual conversion factor should be smaller than what we apply in this work. This can result in the overestimation of the molecular mass by a factor of $\sim$1.5, based on the conversion factors that we apply in Section 3.1. The mass–metallicity relation in galaxy clusters at high redshifts is still controversial; however, several studies suggest that less massive galaxies in high-z galaxy clusters tend to be more metal-rich than the field galaxies, while massive galaxies do not show such a difference between galaxy clusters and fields (Kulas et al. 2013; Shimakawa et al. 2015).

4.2. Comparison with Other Clusters at Similar Redshifts

To discuss how representative the results that we have found are in galaxy clusters at $z \sim 1.5$, we compare with two studies in galaxy clusters at $z \sim 1.6$ (Noble et al. 2017; Rudnick et al. 2017). Noble et al. (2017) detected CO (2–1) emission

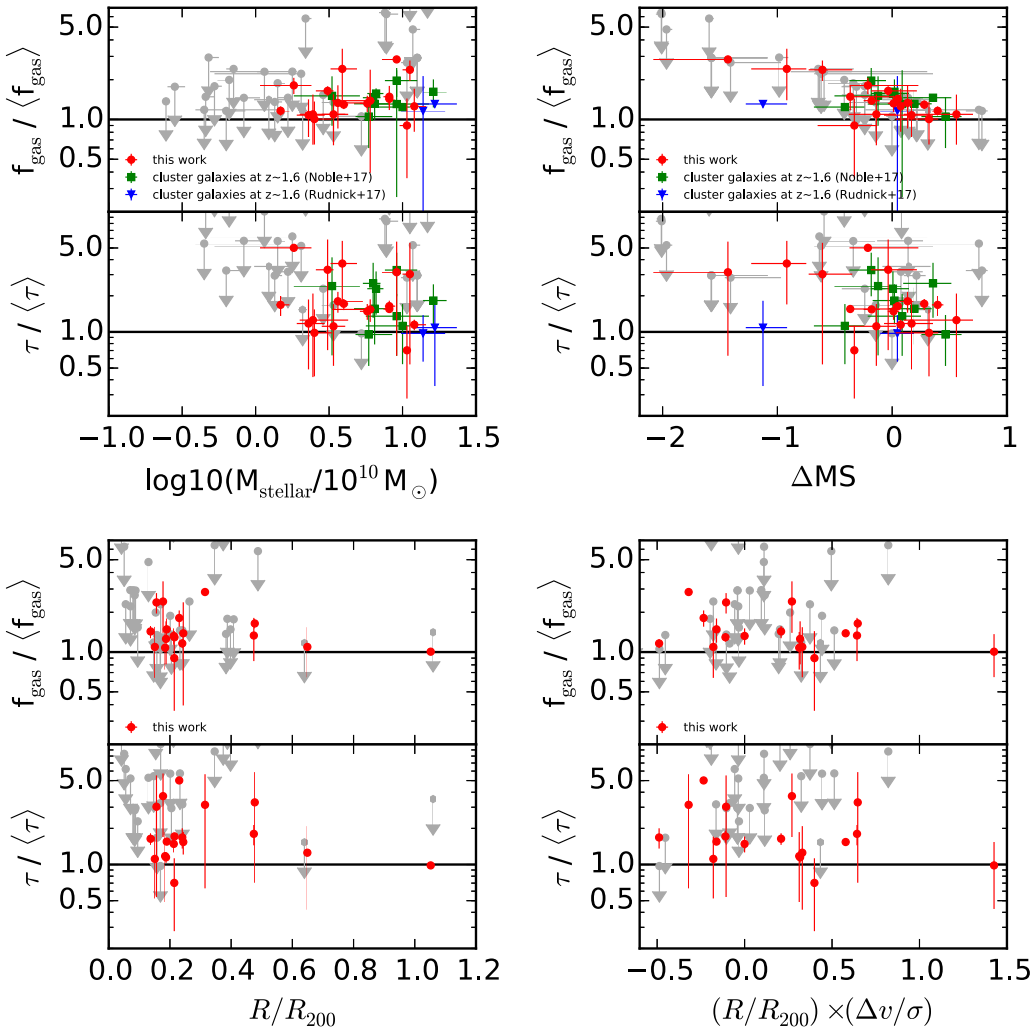

Figure 8. Same as Figure 7, but the gas fraction and depletion time are compared with what is expected from the scaling relations for field galaxies given by Tacconi et al. (2018). The MS is derived from the literature of Speagle et al. (2014). The scaling relations are functions of redshift, stellar mass, and ratio of specific SFR to that of MS galaxies with a given stellar mass at the redshift; thus, they take account of the redshift evolution of the specific SFR. The horizontal line in each panel shows the gas fraction and depletion time on the scaling relations. The red circles show our results. The green squares show the results of Noble et al. (2017) for galaxies in three galaxy clusters at $z \sim 1.6$, and the blue triangles show the results of Rudnick et al. (2017) for galaxies in a galaxy cluster at $z \sim 1.6$.

lines from 11 gas-rich galaxies in three galaxy clusters at $z \sim 1.6$ using ALMA. They argued that the cluster galaxies tend to have enhanced gas fractions compared with the field scaling relations at $z = 1.6$ but depletion timescales consistent with those of the field galaxies. These three clusters are found by the *Spitzer* Adaptation of the Red-sequence Cluster Survey (Muzzin et al. 2009; Wilson et al. 2009). They estimate a cluster mass of $\gtrsim 10^{14}$ $M_\odot$ from the richness of the member galaxies (Noble et al. 2017). Rudnick et al. (2017) detected CO (1–0) emission lines from two massive galaxies in a confirmed $z = 1.62$ galaxy cluster (Papovich et al. 2010; Tanaka et al. 2010) using the Karl G. Jansky Very Large Array (VLA). They argued that the gas fractions and star formation efficiencies of the galaxies in the cluster are comparable to those of the field galaxy scaling relations. The cluster mass is estimated to be 1.1×10^{14} $M_\odot$ from *XMM-Newton* X-ray data (Papovich et al. 2010; Tanaka et al. 2010). Because the cluster mass of the XMMXCS J2215.9–1738 cluster is estimated to be $\sim 3 \times 10^{14}$ $M_\odot$, all of these clusters are systems with a similar mass scale.

The molecular masses for the galaxies associated with the galaxy clusters at $z \sim 1.6$ are derived in the same manner as in Section 3.1 using the information available from the literature (Noble et al. 2017; Rudnick et al. 2017) for proper comparison with our results. We use the stellar masses and SFRs of the galaxies shown in the literature. The comparison with the results in the galaxy clusters at $z \sim 1.6$ shows that our results are consistent with those of the other clusters at similar redshifts (Figure 8). Therefore, we conclude that cluster galaxies at $z \sim 1.5$ can have a molecular gas fraction larger than what the field galaxies have. While the depletion timescale of the massive cluster galaxies with $\sim 10^{11}$ $M_\odot$ is similar to that of the field galaxies, less massive galaxies can have a larger depletion time.

4.3. Molecular Gas Reservoirs of Quiescent Galaxies

The member galaxies with a CO line and/or dust continuum detected are located away from the very center of the cluster (Figure 1). It is worth investigating how much of the gas reservoirs of the member galaxies in the very center is left. To give a constraint on the molecular gas mass for such galaxies, the stacked data in Band 3 are used to discuss the average amount of molecular gas in these member galaxies.

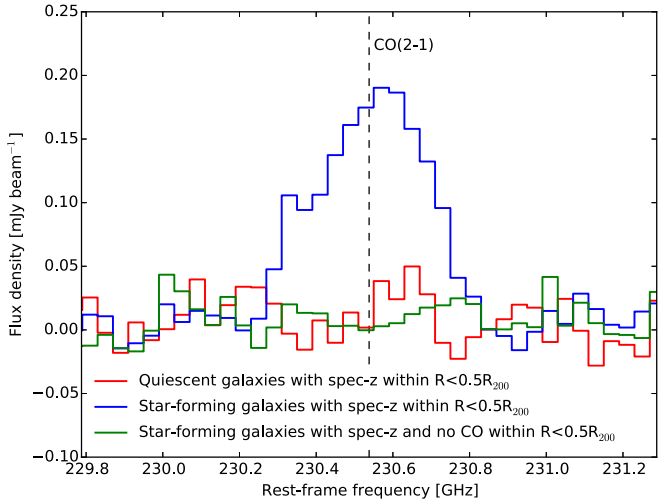

Figure 9. Stacked spectra around $\nu_{\rm rest} = 230.538$ GHz in ALMA Band 3 data for quiescent galaxies (red), star-forming galaxies (blue), and star-forming galaxies without CO detected individually (green) that are spectroscopically confirmed within a radius of $0.5R_{200}$. The dashed line shows a frequency of the CO(2–1) emission line. The quiescent or star-forming galaxies are classified by the $U - V$ and $V - J$ color diagram (Figure 4). The CO(2–1) emission line is not detected from the stacked spectrum of quiescent galaxies. The flux or the upper limit of the flux of the emission line in the stacked spectrum is shown in Table 3.

We stack the Band 3 data for two populations of quiescent and star-forming galaxies that are classified based on the *UVJ* diagram (Figure 4). There are 12 quiescent galaxies and 27 star-forming galaxies that are spectroscopically confirmed within half of R_{200}. Among them, a quiescent galaxy and 15 star-forming galaxies have CO(2–1) lines detected. The redshift confirmation is essential to shift the individual spectrum from the observed frame to the rest frame. Figure 9 shows the stacked spectra for three samples from the two populations: all quiescent galaxies, all star-forming galaxies, and star-forming galaxies without CO(2–1) detection. For the sample of all star-forming galaxies, since about half of them have CO(2–1) lines detected individually, the CO(2–1) line is also detected in the stacked spectrum. On the other hand, the stacked spectra of the quiescent and star-forming galaxies without CO detected individually show no detection of the CO(2–1) line. Using the intensity map integrated in velocity by 400 km s^{-1}, the average CO(2–1) line flux and the 5σ upper limit flux are estimated for the star-forming and quiescent galaxies, respectively. We then convert them to the molecular gas masses in the same manner as in Section 3.1. Note that we make sure of the validity of our procedure by stacking the data for the member galaxies with CO(2–1) detected individually. The measurements from the stacked spectra are shown in Table 3.

The upper limit of molecular gas for the quiescent galaxies shows the gas fraction of <0.08 and the depletion timescale of <9.8 Gyr, suggesting that the quiescent galaxies in the center consume most of their molecular gas. On the other hand, star-forming galaxies still have enough gas to keep forming stars. However, many star-forming galaxies in the cluster have larger gas reservoirs compared with the field galaxies (Section 4.1), and they also show a larger depletion time as they deviate from the MS. This may imply that it is difficult to consume the molecular gas only by star formation. Starvation to stop the supply of gas to the cluster galaxies, as well as ram pressure to strip gas from the galaxies, may be required to effectively reduce the amount of the molecular gas, which can accelerate the growth of cluster galaxies to become quiescent galaxies in the cluster core. Indeed, it is observed that the molecular and H I gas are stripped from the galaxies by ram pressure in the local galaxy cluster (Sivanandam et al. 2010; Jáchym et al. 2014). Also, virial shock in the massive halo of this cluster at $z = 1.46$ would prevent the cold gas stream from accreting to the member galaxies settled in the cluster center (Birnboim & Dekel 2003; Dekel & Birnboim 2006). Another possibility is galaxy mergers. The merging of gas-rich galaxies can induce a starburst in the galaxy center (Hopkins et al. 2008), which results in consumption of gas reservoirs. The stellar masses of the gas-rich galaxies in this cluster are comparable to and/or a factor of $\sim$2–5 smaller than those of quiescent galaxies. A perspective of mass growth supports that the merging is one of the possible processes. The feedback from AGNs and SNe can also have a role in the quenching mechanism. Outflows of massive molecular gas by AGNs and SNe are observed from ultraluminous infrared galaxies in the local universe (Feruglio et al. 2010; Sturm et al. 2011; Cicone et al. 2014). Since there is no evidence that a high fraction of the starburst galaxies and AGNs are found in this cluster, the feedback may be an inadequate process for environmental effects on the transition of star-forming galaxies to quiescent galaxies in galaxy clusters. However, it would be one of the important processes not only to reduce the efficiency of star formation but also to blow the gas off from the galaxies.

There are a few previous studies that show a constraint on the molecular gas fraction for quiescent galaxies at similar redshifts. Sargent et al. (2015) presented the upper limit of CO(2–1) luminosity in early-type galaxies at $z = 1.43$ with the IRAM/Plateau de Bure Interferometer (PdBI), which shows that the 3σ upper limit of the gas fraction is $\lesssim$10%. Gobat et al. (2018) used the stacked SED ranging from MIR to radio for about 1000 early-type galaxies at $\langle z \rangle = 1.76$ to give a constraint on their molecular gas reservoirs. The gas mass is derived from the dust mass that is estimated from the SED under the assumption of a metallicity-dependent gas-to-dust ratio. They derived the gas fraction of $\sim$13%. Note that the stellar masses shown in the literature are converted to those with a Chabrier (2003) IMF. The gas fraction that we derive for the quiescent galaxies in the galaxy cluster at $z = 1.46$ is similar to those for the field quiescent galaxies at similar redshifts, suggesting that quiescent galaxies consume the fuel of gas down to a similarly low level of $\lesssim$10% irrespective of the environment. However, the ATLAS^{3D} project shows that the early-type galaxies in the local universe have a gas fraction that is an order of magnitude smaller than that for the galaxies at $z \sim 1.5$ (Young et al. 2011). Preferably, the local post-starburst galaxies seem to have a gas fraction similar to that of the high-z cluster quiescent galaxies (French et al. 2015).

5. Summary and Conclusions

We conduct the ALMA observations in Band 3 and Band 7 in the X-ray galaxy cluster XMMXCS J2215.9–1738 at $z = 1.46$. While the Band 3 data allow us to detect CO(2–1) emission lines from cluster member galaxies, the Band 7 data allow us to detect dust continuum emissions at 870 μm. We use these ALMA data to investigate molecular gas reservoirs in the member galaxies within a clustercentric radius of $\sim R_{200}$ and then discuss the evolution of their star formation activities in terms of star formation efficiency and gas consumption.

Table 3
Average Properties of the Confirmed Member Galaxies within Half of R_{200} Obtained from Stacked Spectra in Band 3

	Number[a]		$\langle M_{\rm stellar}\rangle$[b] ($10^{10}\,M_\odot$)	$\langle {\rm SFR}\rangle$[b] ($M_\odot\ {\rm yr}^{-1}$)	$S\Delta v$[c] (Jy km s^{-1})	$M_{\rm gas,CO}$ ($10^{10}\,M_\odot$)	$f_{\rm gas}$	τ (Gyr)
Quiescent	12	(1)	11.0	1	<0.07	<0.93	<0.08	<9.78
Star-forming	27	(15)	2.3	31	0.21	3.83	0.63	1.24
Star-forming w/o CO	12	(0)	0.6	7	<0.04	<1.05	<0.62	<1.58

Notes.
[a] The number of galaxies stacked. The values in parentheses are the number of galaxies with CO(2–1) detected individually.
[b] The median values in the samples.
[c] Estimated from the intensity map integrated in velocity by 400 km s^{-1}.

Hayashi et al. (2017) already reported the discovery of 17 CO(2–1) emission lines associated with the cluster. In this paper, we newly detect nine 870 μm sources in the Band 7 data. Although one source is a foreground galaxy, the other eight galaxies are confirmed to be cluster member galaxies. Seven galaxies have both CO(2–1) lines and dust continuum emissions detected, and the position of the dust continuum emission is consistent with that of the CO(2–1) emission. Consequently, we have CO(2–1) emission lines and/or dust continuum emissions from 18 member galaxies within $\sim R_{200}$. The rest-frame $U-V$ versus $V-J$ color diagram shows that most of the CO lines and/or dust emissions are detected from dusty star-forming galaxies.

We derive the molecular gas masses from the CO luminosities using the metallicity-dependent (i.e., stellar mass–dependent) conversion factors (Tacconi et al. 2018), as well as dust continuum luminosities according to Scoville et al. (2016), while taking into account the metallicity dependency of the dust-to-gas ratio. The molecular gas masses derived from the two ways are consistent with each other.

We investigate the gas fraction and depletion timescale as a function of stellar mass, offset from the MS of star-forming galaxies, clustercentric radius, and accretion phase. The galaxies with larger SFRs at a given stellar mass show a larger gas fraction and smaller depletion timescale. There is no strong dependence of gas fraction and depletion time on the clustercentric radius and accretion phase. The cluster member galaxies with CO and/or dust continuum detected tend to have a larger gas fraction and depletion time, compared with those from the scaling relations for field galaxies. If infalling regions and filaments around galaxy clusters help feed the gas through inflow to member galaxies, the cluster galaxies can have larger gas reservoirs than the field galaxies at $z\sim 1.5$. Nevertheless, the cluster galaxies must become more inefficient in star formation than field galaxies. As the member galaxies are infalling closer to the center, the deviation of the gas fraction and depletion time from the scaling relations seems to get larger. Therefore, some environmental effects peculiar to galaxies associated with galaxy clusters may reduce the efficiency of star formation.

Massive quiescent galaxies in the cluster core no longer have large gas reservoirs and efficient star formation. We stack the Band 3 spectra for 12 quiescent galaxies within a radius of 0.5 R_{200}. However, no CO(2–1) emission line is detected from the stacked spectrum. The upper limits of the molecular gas and molecular gas fraction are estimated to be $\lesssim 10^{10}\ M_\odot$ and $\lesssim$10%, respectively, which are similar to those for quiescent galaxies in general fields at similar redshifts. This suggests that irrespective of the environment, the massive quiescent galaxies consume most of the fuel of gas and evolve passively in the center of the cluster. We speculate that since cluster member galaxies are subject to additional environmental effects, such as ram pressure, starvation, and merging, compared with field galaxies, cluster galaxies are easier to reduce gas reservoirs and then quench star formation, which results in a larger fraction of quiescent galaxies in galaxy clusters than in general fields.

We thank the anonymous referee for providing constructive comments and suggestions. M.H. acknowledges financial support by JSPS Grant-in-Aid for Young Scientists (A) grant Number JP26707006 and was also supported by the ALMA Japan Research Grant of the NAOJ Chile Observatory, NAOJ-ALMA-180. K.K. acknowledges financial support by the JSPS Grant-in-Aid for Scientific Research (A) JP25247019. Y.Y. is thankful for the JSPS fellowship. This paper makes use of the following ALMA data: ADS/JAO.ALMA#2011.1.00623.S and ADS/JAO.ALMA#2015.1.00779.S. ALMA is a partnership of the ESO, NSF (USA), and NINS (Japan), together with the NRC (Canada), NSC and ASIAA (Taiwan), and KASI (Republic of Korea), in cooperation with the Republic of Chile. The Joint ALMA Observatory is operated by the ESO, AUI/NRAO, and NAOJ. This work uses the data collected at the Subaru Telescope, which is operated by the National Astronomical Observatory of Japan. This work also uses data based on observations obtained with the MegaPrime/MegaCam, a joint project of the Canada–France–Hawaii Telescope (CFHT) and CEA/IRFU, at the CFHT, which is operated by the National Research Council (NRC) of Canada, the Institut National des Science de l'Univers of the Centre National de la Recherche Scientifique (CNRS) of France, and the University of Hawaii. This work is based in part on data products produced at Terapix, available at the Canadian Astronomy Data Centre as part of the Canada–France–Hawaii Telescope Legacy Survey, a collaborative project of NRC and CNRS. Some of the data presented in this paper were obtained from the Mikulski Archive for Space Telescopes (MAST). STScI is operated by the Association of Universities for Research in Astronomy, Inc., under NASA contract NAS5-26555. Support for MAST for non-*HST* data is provided by the NASA Office of Space Science via grant NNX09AF08G and by other grants and contracts.

Facilities: ALMA, Subaru, CFHT, *HST*.

ORCID iDs

Masao Hayashi https://orcid.org/0000-0002-9321-7406
Ken-ichi Tadaki https://orcid.org/0000-0001-9728-8909
Kotaro Kohno https://orcid.org/0000-0002-4052-2394
Yuki Yamaguchi https://orcid.org/0000-0002-7019-4010
Bunyo Hatsukade https://orcid.org/0000-0001-6469-8725

Rhythm Shimakawa https://orcid.org/0000-0003-4442-2750
Yoichi Tamura https://orcid.org/0000-0003-4807-8117
Tomoko L. Suzuki https://orcid.org/0000-0002-3560-1346

References

Aravena, M., Carilli, C. L., Salvato, M., et al. 2012, MNRAS, 426, 258
Barro, G., Kriek, M., Pérez-González, P. G., et al. 2016, ApJL, 827, L32
Beifiori, A., Mendel, J. T., Chan, J. C. C., et al. 2017, ApJ, 846, 120
Bertin, E., & Arnouts, S. 1996, A&AS, 117, 393
Bielby, R., Hudelot, P., McCracken, H. J., et al. 2012, A&A, 545, A23
Birnboim, Y., & Dekel, A. 2003, MNRAS, 345, 349
Bolatto, A. D., Wolfire, M., & Leroy, A. K. 2013, ARA&A, 51, 207
Brammer, G. B., Whitaker, K. E., van Dokkum, P. G., et al. 2011, ApJ, 739, 24
Bruzual, G., & Charlot, S. 2003, MNRAS, 344, 1000
Calzetti, D., Armus, L., Bohlin, R. C., et al. 2000, ApJ, 533, 682
Cardelli, J. A., Clayton, G. C., & Mathis, J. S. 1989, ApJ, 345, 245
Carilli, C. L., & Walter, F. 2013, ARA&A, 51, 105
Carniani, S., Marconi, A., Maiolino, R., et al. 2017, A&A, 605, A105
Casasola, V., Magrini, L., Combes, F., et al. 2013, A&A, 558, A60
Chabrier, G. 2003, PASP, 115, 763
Chapman, S. C., Bertoldi, F., Smail, I., et al. 2015, MNRAS, 449, L68
Chen, C.-C., Hodge, J. A., Smail, I., et al. 2017, ApJ, 846, 108
Cicone, C., Maiolino, R., Sturm, E., et al. 2014, A&A, 562, A21
Daddi, E., Dickinson, M., Morrison, G., et al. 2007, ApJ, 670, 156
Dannerbauer, H., Lehnert, M. D., Emonts, B., et al. 2017, A&A, 608, A48
Decarli, R., Walter, F., Manuel, A., et al. 2016a, ApJ, 833, 69
Decarli, R., Walter, F., Manuel, A., et al. 2016b, ApJ, 833, 70
Dekel, A., & Birnboim, Y. 2006, MNRAS, 368, 2
Dressler, A., Oemler, A., Jr., Couch, W. J., et al. 1997, ApJ, 490, 577
Elbaz, D., Daddi, E., Le Borgne, D., et al. 2007, A&A, 468, 33
Feruglio, C., Maiolino, R., Piconcelli, E., et al. 2010, A&A, 518, L155
French, K. D., Yang, Y., Zabludoff, A., et al. 2015, ApJ, 801, 1
Fujimoto, S., Ouchi, M., Ono, Y., et al. 2016, ApJS, 222, 1
Geach, J. E., Smail, I., Moran, S. M., et al. 2011, ApJL, 730, L19
Genzel, R., Tacconi, L. J., Combes, F., et al. 2012, ApJ, 746, 69
Genzel, R., Tacconi, L. J., Lutz, D., et al. 2015, ApJ, 800, 20
Gobat, R., Daddi, E., Magdis, G., et al. 2018, NatAs, 2, 239
Hatsukade, B., Kohno, K., Umehata, H., et al. 2016, PASJ, 68, 36
Hayashi, M., Kodama, T., Kohno, K., et al. 2017, ApJL, 841, L21
Hayashi, M., Kodama, T., Koyama, Y., et al. 2010, MNRAS, 402, 1980
Hayashi, M., Kodama, T., Koyama, Y., et al. 2014, MNRAS, 439, 2571
Hayashi, M., Kodama, T., Koyama, Y., Tadaki, K.-I., & Tanaka, I. 2011, MNRAS, 415, 2670
Hilton, M., Lloyd-Davies, E., Stanford, S. A., et al. 2010, ApJ, 718, 133
Hodge, J. A., Swinbank, A. M., Simpson, J. M., et al. 2016, ApJ, 833, 103
Hopkins, P. F., Hernquist, L., Cox, T. J., & Kereš, D. 2008, ApJS, 175, 356
Ikarashi, S., Ivison, R. J., Caputi, K. I., et al. 2015, ApJ, 810, 133
Ivison, R. J., Swinbank, A. M., Smail, I., et al. 2013, ApJ, 772, 137
Jáchym, P., Combes, F., Cortese, L., Sun, M., & Kenney, J. D. P. 2014, ApJ, 792, 11
Jaffé, Y. L., Smith, R., Candlish, G. N., et al. 2015, MNRAS, 448, 1715
Kakkad, D., Mainieri, V., Brusa, M., et al. 2017, MNRAS, 468, 4205
Kennicutt, R. C., & Evans, N. J. 2012, ARA&A, 50, 531
Kennicutt, R. C., Jr. 1998, ApJ, 498, 541
Koyama, S., Koyama, Y., Yamashita, T., et al. 2017, ApJ, 847, 137
Koyama, Y., Smail, I., Kurk, J., et al. 2013, MNRAS, 434, 423
Kriek, M., van Dokkum, P. G., Labbé, I., et al. 2009, ApJ, 700, 221
Kulas, K. R., McLean, I. S., Shapley, A. E., et al. 2013, ApJ, 774, 130
Labbé, I., Huang, J., Franx, M., et al. 2005, ApJL, 624, L81
Lee, M. M., Tanaka, I., Kawabe, R., et al. 2017, ApJ, 842, 55
Ma, C.-J., Smail, I., Swinbank, A. M., et al. 2015, ApJ, 806, 257
Madau, P., & Dickinson, M. 2014, ARA&A, 52, 415
Magnelli, B., Elbaz, D., Chary, R. R., et al. 2009, A&A, 496, 57
Magnelli, B., Saintonge, A., Lutz, D., et al. 2012, A&A, 548, A22
Maíz Apellániz, J. 2006, AJ, 131, 1184
McMullin, J. P., Waters, B., Schiebel, D., Young, W., & Golap, K. 2007, in ASP Conf. Ser. 376, Astronomical Data Analysis Software and Systems XVI, ed. R. A. Shaw, F. Hill, & D. J. Bell (San Francisco, CA: ASP), 127
Muzzin, A., van der Burg, R. F. J., McGee, S. L., et al. 2014, ApJ, 796, 65
Muzzin, A., Wilson, G., Yee, H. K. C., et al. 2009, ApJ, 698, 1934
Noble, A. G., McDonald, M., Muzzin, A., et al. 2017, ApJL, 842, L21
Noble, A. G., Webb, T. M. A., Muzzin, A., et al. 2013, ApJ, 768, 118
Noble, A. G., Webb, T. M. A., Yee, H. K. C., et al. 2016, ApJ, 816, 48
Noeske, K. G., Weiner, B. J., Faber, S. M., et al. 2007, ApJL, 660, L43
Papovich, C., Momcheva, I., Willmer, C. N. A., et al. 2010, ApJ, 716, 1503
Peng, Y.-J., Lilly, S. J., Kovač, K., et al. 2010, ApJ, 721, 193
Renzini, A., & Peng, Y.-J. 2015, ApJL, 801, L29
Rudnick, G., Hodge, J., Walter, F., et al. 2017, ApJ, 849, 27
Saintonge, A., Catinella, B., Cortese, L., et al. 2016, MNRAS, 462, 1749
Saintonge, A., Catinella, B., Tacconi, L. J., et al. 2017, ApJS, 233, 22
Saintonge, A., Lutz, D., Genzel, R., et al. 2013, ApJ, 778, 2
Saintonge, A., Tacconi, L. J., Fabello, S., et al. 2012, ApJ, 758, 73
Sargent, M. T., Daddi, E., Béthermin, M., et al. 2014, ApJ, 793, 19
Sargent, M. T., Daddi, E., Bournaud, F., et al. 2015, ApJL, 806, L20
Schmidt, M. 1959, ApJ, 129, 243
Schreiber, C., Pannella, M., Elbaz, D., et al. 2015, A&A, 575, A74
Scoville, N., Arnouts, S., Aussel, H., et al. 2013, ApJS, 206, 3
Scoville, N., Lee, N., Vanden Bout, P., et al. 2017, ApJ, 837, 150
Scoville, N., Sheth, K., Aussel, H., et al. 2016, ApJ, 820, 83
Seko, A., Ohta, K., Yabe, K., et al. 2016, ApJ, 819, 82
Shimakawa, R., Kodama, T., Tadaki, K.-I., et al. 2015, MNRAS, 448, 666
Silverman, J. D., Daddi, E., Rodighiero, G., et al. 2015, ApJL, 812, L23
Simpson, J. M., Smail, I., Swinbank, A. M., et al. 2015, ApJ, 807, 128
Sivanandam, S., Rieke, M. J., & Rieke, G. H. 2010, ApJ, 717, 147
Sobral, D., Stroe, A., Koyama, Y., et al. 2016, MNRAS, 458, 3443
Speagle, J. S., Steinhardt, C. L., Capak, P. L., & Silverman, J. D. 2014, ApJS, 214, 15
Stach, S. M., Swinbank, A. M., Smail, I., et al. 2017, ApJ, 849, 154
Stanford, S. A., Romer, A. K., Sabirli, K., et al. 2006, ApJL, 646, L13
Sturm, E., González-Alfonso, E., Veilleux, S., et al. 2011, ApJL, 733, L16
Tacconi, L. J., Genzel, R., Neri, R., et al. 2010, Natur, 463, 781
Tacconi, L. J., Genzel, R., Neri, R., et al. 2013, ApJ, 768, 74
Tacconi, L. J., Genzel, R., Saintonge, A., et al. 2018, ApJ, 853, 179
Tadaki, K.-I., Kodama, T., Tamura, Y., et al. 2014, ApJL, 788, L23
Tadaki, K.-I., Kohno, K., Kodama, T., et al. 2015, ApJL, 811, L3
Tadaki, K.-I., Kohno, K., Kodama, T., et al. 2017, ApJ, 834, 135
Tanaka, M., Finoguenov, A., & Ueda, Y. 2010, ApJL, 716, L152
Wagg, J., Pope, A., Alberts, S., et al. 2012, ApJ, 752, 91
Walter, F., Decarli, R., Sargent, M., et al. 2014, ApJ, 782, 79
Wang, T., Elbaz, D., Daddi, E., et al. 2016, ApJ, 828, 56
Webb, T. M. A., Lowenthal, J., Yun, M., et al. 2017, ApJL, 844, L17
Whitaker, K. E., Franx, M., Leja, J., et al. 2014, ApJ, 795, 104
Whitaker, K. E., Pope, A., Cybulski, R., et al. 2017, ApJ, 850, 208
Williams, J. P., de Geus, E. J., & Blitz, L. 1994, ApJ, 428, 693
Williams, R. J., Quadri, R. F., Franx, M., van Dokkum, P., & Labbé, I. 2009, ApJ, 691, 1879
Wilson, G., Muzzin, A., Yee, H. K. C., et al. 2009, ApJ, 698, 1943
Wong, O. I., Kenney, J. D. P., Murphy, E. J., & Helou, G. 2014, ApJ, 783, 109
Wuyts, S., Förster Schreiber, N. M., Lutz, D., et al. 2011, ApJ, 738, 106
Wuyts, S., Labbé, I., Förster Schreiber, N. M., et al. 2008, ApJ, 682, 985
Young, L. M., Bureau, M., Davis, T. A., et al. 2011, MNRAS, 414, 940